An Autonomous Aerial Robot with Integrated Delta Manipulator for Aerial Repair

P. Chermprayong, K. Zhang, *Member, IEEE,* F. Xiao and M. Kovac

***Abstract*—Unmanned Aerial Vehicles (UAVs) are capable of entering hazardous areas and accessing hard-to-reach locations at high altitude. However, small-scale UAVs are inherently unstable when exposed to challenging environments. Additionally, their capability to interact with infrastructure with high accuracy is limited due to the need to stabilize the vehicle precisely in flight. To address these challenges, this article introduces a new aerial robotic system with an integrated light-weight Delta manipulator and a kinematics-based approach allowing it to compensate fluctuations of the quadrotor platform due to wind or flight imprecision. Integrating onboard visual-inertial (VI) odometry-aided navigation, the system is characterised in various operation modes, including hovering in windy conditions. The end-effector accuracy of the integrated aerial robot is analysed and compared to the flight accuracy of the quadrotor platform using a 3D motion capture system for ground truthing. The results reveal that the end-effector of the aerial robot achieves a maximum decrease of the root-mean-square-error (RMSE) of 76.4%, 44.1% and 35.8% in X, Y and Z directions respectively in VI odometry-aided tests with 1 m/s wind along Y direction. In the same tests, the maximum fluctuations decrease by 52.8%, 46.9% and 33.6% in the directions of X, Y and Z. As a demonstration of the utility of this stabilised manipulator, we present the design of an on-board extrusion system that can deposit two component LD40 polyurethane foam for precise spot repairs. We selected the LD40 foam as the amorphous repair material due to its substantial expansion rates after deposition that allows for effective area coverage with little material carried on-board. We then demonstrate a complete aerial repair mission for sealing cracks and holes on a section of a standard oil pipe, by autonomously depositing the two component foam on the damaged areas. This work will enable a number of potential applications, including aerial repair at high altitude where access is difficult for ground vehicles and dangerous for human workers.**

***Index Terms*—Aerial Robot, parallel manipulator, aerial repair, kinematics, compensation, visual-inertial odometry-aided navigation.**

I. Introduction

MULTIROTOR UAVs are already used worldwide in many real-world applications [1], [2], [3] such as aerial photography, infrastructure inspection, delivery, smart agriculture, and surveillance .

With the ever-growing demands in the market for multirotor UAVs, the flight controllers, communication and navigation systems, and other smart features have advanced dramatically in recent years. Unlike ground robots[4], multirotor UAVs are still very limited in their ability to hold their spacial position precisely in windy conditions or close to infrastructure elements. This dramatically limits their usability in applications such as aerial manipulation and aerial repair. In order to expand the current capabilities of multirotor UAVs to applications that require precise aerial station-holding, these issues must be addressed. An on-going research theme is to equip flying agents with additional degrees of freedom by integrating robotic manipulators [5], [6], [7], [8].

Given the limited payload of most aerial robots, particularly multirotor UAVs, low-complexity and light-weight grippers were developed for grasping [9], [10], [11], perching and transporting payloads [12]. Due to the low-complexity of these grippers, a relatively simple control system can be effective for manipulator control. Since the grippers in these examples are mounted directly onto the UAVs , they cannot compensate for undesired movement of the aerial platform. UAVs therefore require extremely precise flight control for accurate operations.

In comparison to rigid connections, adding a serial manipulator between the gripper and the UAV platform allows the gripper to be controllable and relatively flexible [13], [14], [15]. However, the position and orientation of each joint on the aerial-serial link cause substantial disturbance to the dynamics of the UAV due to the out-of-balance masses.

In contrast to the serial manipulators, parallel manipulators in general have a high power-to-weight ratio and can drive the end-effector at high velocity and acceleration [16], [17]. Errors in the joint positioning of this type of manipulator become averaged rather than accumulated in serial manipulator cases. This type of manipulator therefore can yield better accuracy than serial manipulators [18]. Furthermore, the actuators for a parallel robot are fixed at its base, which can be mounted directly on the UAV frame, reducing disturbance to the dynamics of the UAV.

An integrated parallel manipulator can enable new applications for UAVs, such as aerial object manipulation [19] and aerial repair [20], [21].

Focusing on the implementation of high-precision tasks for parallel manipulators in real-world application for aerial repair, this paper presents a new aerial robotic system that integrates a Delta manipulator [22], [23] and a quadrotor UAV (Fig.1).

In this work, we propose a control architecture for the integrated aerial robotic system and verify the control algorithm to be effective for autonomous aerial repair. We quantitatively analyse the controller performance with experimental results obtained using a motion capture system for ground truthing, showing that the proposed aerial robot is capable of performing high-precision operations with the integrated Delta manipulator and extrusion system. The contributions of this paper are the following:

1) To the best of our konwledge, this work presents the first aerial robot capable of depositing liquid expansion foam

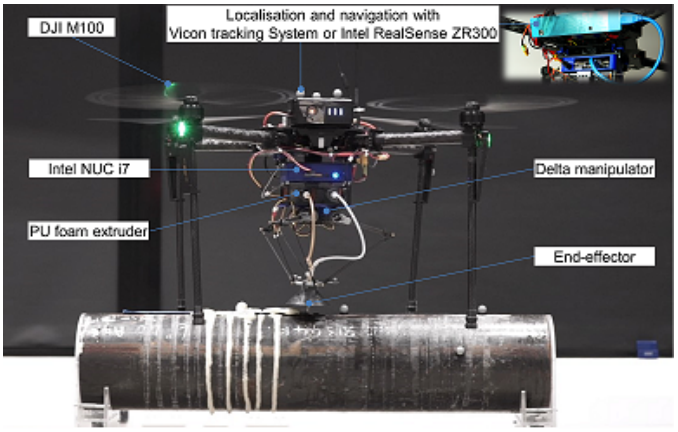

Fig. 1. The autonomous aerial robot with onboad Intel RealSense VI sensor, Intel NUC i7 processor and integrated Delta manipulator for aerial repair tasks.

using a high-precision and light-weight 3-DOF Delta manipulator for aerial repair work.
2) Characterisation of the end-effector accuracy and the improvement that is achieved by compensating the quadrotor fluctuations with the Delta arm manipulator.
3) Development of a light-weight extrusion system for extrusion of liquid expansion foam for aerial repair.
4) A demonstration of aerial pipeline repair using visual-inertial (VI) odometry-aided navigation.

In the following section we will introduce the aerial robot, which consists of a quadrotor UAV, a customised 3-DOF Delta parallel manipulator, an off-the-shelf VI sensor and an onboard computer. Section III will present the control architecture of the integrated robotic system. Section IV will follow with the experimental characterization and validation of the proposed system for accurate operations, which uses its onboard visual-inertial odometry system for navigation. Section V will demonstrate the application of aerial repair for sealing cracks on oil and gas pipes using an amorphous construction and repair material. The future potential of bringing this robotic system into outdoor environments by using visual-inertial guidance is discussed in Section VI. This paper is then concluded in Section VII.

II. The New Aerial Robot with Integrated Delta Manipulator: System Description

A. The Matrice 100 Platform

In this work we use DJI Matrice 100 (M100) as the quadrotor platform. It has a kerb weight of 2.431 kg with a TB48D battery, a maximum take-off weight of 3.6 kg, a diagonal wheelbase of 650 mm and a hovering time of 16 minutes with 1kg payload when the TB48D battery is in use. This allows for 1.169 kg of payload before the UAV reaches its maximum take-off weight. The detailed specs and CAD model of the M100 quadrotor is documented and available from the official website.

B. The Delta Manipulator

The employed Delta manipulator, which is capable of 3-DOF pure translational motion, is one of the most used parallel robot in production. The parallel robot has three identical limbs, as seen in Fig. 2, and employs only revolute joints. The revolute joints connecting the three limbs to the base and platform are located at B_i and D_i (i = 1, 2 and 3),which are vertices of the two virtual equilateral triangles and define the geometrical parameters of the base and platform respectively. Each limb contains an upper arm B_iC_i and a lower parallelogram 4R linkage C_iD_i.

The base and platform are defined by the circumradius R and r of the virtual equilateral triangles $\triangle B_1B_2B_3$ and $\triangle D_1D_2D_3$. The design parameters for the upper and lower arms are denoted by L and l as illustrated in Fig. 2.

The three revolute joints connected to the base at points B_i are actuated by three servos, and the angular inputs θ_i are measured from the base plane to the upper arm B_iC_i.

A coordinate frame $\{\mathbb{A}\}$ for the Delta manipulator is set with its origin A attached to the geometric centre of the base. The x_A- and z_A-axis are located in the base plane with z_A-axis parallel to line B_2B_3, Whilst y_A-axis is perpendicular to the base plane and forms a right-handed coordinate frame.

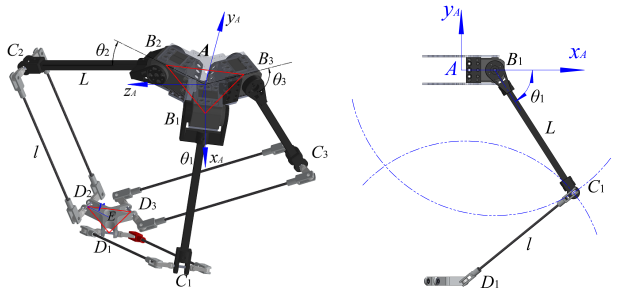

Fig. 2. 3D model of the Delta manipulator employs purely revolute joints.

1) Forward kinematics: The forward kinematics of the Delta manipulator can be solved using a geometrical method [24]. As the base and end-effector always remain in the same orientation, it only allows the end-effector to move in translational motion. The point C_i of each limb traces an virtual sphere with the centre located at D_i and radius l. By offsetting these spheres towards the centre of the manipulator, in the same plane that is defined by its upper and lower limb, we get three spheres at known centres and known radii. The intersection point, $E_0(x_t, y_t, z_t)$, can be found by solving three intersecting quadratic sphere equations given by

$$(x_t - x_i)^2 + (y_t - y_i)^2 + (z_t - z_i)^2 = l^2 \quad (1)$$

where i = 1,2,3 and (x_i,y_i,z_i) is the centre of ith sphere and l is the length of the lower arm, parallelogram 4R linage.

If all these spheres intersect tangentially, it yields one solution. However, it will not yield any solutions if these spheres do not intersect. Geometrically, a system of three intersecting spheres can yield two solutions. From the fact that the Delta manipulator in Fig. 2 always has its end-effector positioned below its base, solutions that give the end effector position above its base are eliminated.

2) Inverse kinematics: The inverse kinematics of the Delta manipulator is to derive the angular inputs θ_i from the position of a given configuration of the end-effector. In each limb of the Delta manipulator, the parallelogram 4R linkage together with the two revolute joints at point C_i and D_i are equivalent to a UU chain. It implies that point C_i is moving on a sphere with the centre D_i and radius l as illustrated in Fig. 2(b). Taking this geometric property of the Delta manipulator, a geometric method [25] is used for solving the inverse kinematics. The angular input θ_1 required to configure the end-effector to a given position vector $E_0 = [x_t, y_t, z_t]^{\mathrm{T}}$ is calculated by

$$\theta_1 = arctan(z_{c1})/(y_{b1} - y_{c1}) \tag{2}$$

in which z_{c1}, y_{b1} and z_{b1} are the elements of the position vector of points B_1 and C_1 in the reference frame $A - x_1y_1z_1$ and can be derived by solving

$${z_{c1}}^2 = L^2 - (y_{c1} + R)^2 \tag{3}$$

and

$$l^2 - {x_0}^2 = (y_{c1} - (y_0 - r))^2 + (z_{c1} - z_0)^2 \tag{4}$$

The other two angular inputs θ_2 and θ_3 can also be calculated independently with the same method as above.

3) Reachable and executed workspaces: With the solution for kinematics as outlined above, the reachable workspace of the Delta manipulator is analysed with the design parameters then determined by enabling the Delta manipulator to compensate for the fluctuation of the aerial platform, with DJI M100 employed in this work.

Given the errors between the reference and actual trajectory of the DJI M100 during autonomous flight reported in [26], the reachable workspaces with various values for design parameters are analysed and compared to the trajectory fluctuations of M100 and the selected values for these parameters of R = 37 mm, r = 20.5 mm, L = 101.5 mm and l = 150.5 mm. With these values selected for the design parameters, Fig. 3 illustrates both the reachable workspace computed for forward kinematics and executable workspace to compensate the UAV's fluctuation.

4) Inverse kinematics-based method for compensating the UAV's fluctuation: As illustrated in Fig. 1, the Delta arm base is fixed to the floating UAV frame while the end-effector is capable of 3-DOF translational motion with respect to the UAV frame. A simplified schematic model of the system is illustrated in Fig.4. The body frame $\{\mathbb{O}\}$ of the aerial robot is attached at the geometric center of the UAV with X-axis pointing in the forward direction of the UAV, the Z-axis is perpendicular to the UAV frame and Y-axis points to the left-hand slide to form a right-handed frame. The local frame $\{\mathbb{A}\}$ of Delta manipulator is parallel to the body frame $\{\mathbb{O}\}$ with its origin attached at the center A of Delta manipulator base. The offset between the two centres O and A is denoted by b. At the other end of the Delta manipulator, the end-effector with centre T is directly mounted underneath the moving platform of Delta manipulator and the distance between centres E and T is denoted by f.

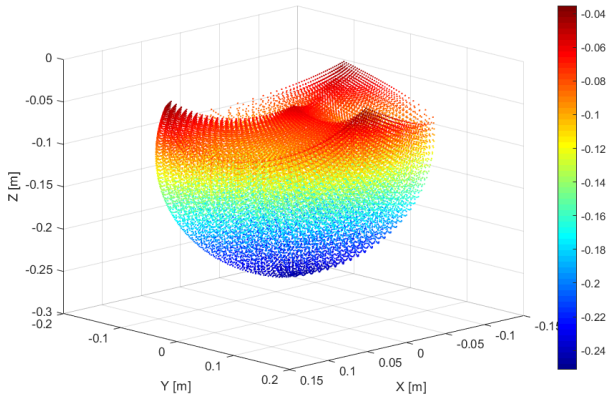

Fig. 3. Reachable workspace of the Delta manipulator. The colour-bar shows distances in Z-axis between the base of the Delta manipulator to reachable end effector location.

With the coordinate systems in Fig. 4, a unit-vector quaternion representing rotation from world frame $\{\mathbb{W}\}$ to the body frame $\{\mathbb{O}\}$ of the UAV is given by $\mathbf{Q}_O = [w_o, x_o, y_o, z_o]^{\mathrm{T}} = [1,0,0,0]^{\mathrm{T}}$, in which w_o is the real part and x_o, y_o and z_o are the vector part of the quaternion.

In order to position the centre T precisely at a target point, the optimized solution is to hover the UAV directly above the target point so that ET is vertically aligned with Z-axis.

However, a flying UAV in real world scenarios is a floating platform with both translation and orientation offsets from the optimized solution. In such cases, the moving platform of the Delta manipulator has to move correspondingly with respect to the body frame $\{\mathbb{O}\}$ to allow the the centre T of the end-effector to be at the target point, thereby compensating the offset of the UAV platform.

When the UAV platform drifts to the position at O' (Fig.4) with a purely translation offset, the position vector of centre A in the frame $\{\mathbb{O}'\}$ is expressed as $\overline{O'A'} = [0,0,-b]$. With further orientation offset of the UAV frame at position O', centre A moves to point A''. The new position vector $\overline{O'A''}$ is calculated as

$$\overline{O'A''} = \mathbf{Q}_{O'}\ \overline{O'A'}\ \overline{\mathbf{Q}}_{O'} \tag{5}$$

where $\overline{\mathbf{Q}}_{O'}$ is a conjugate of quaternion $\mathbf{Q}_{O'}$.

Given the capability of the pure translation of the moving platform with respect to the base of the Delta manipulator, it derives

$$\overline{E''T} = \mathbf{Q}_{O'}\ \overline{ET}\ \overline{\mathbf{Q}}_{O'}. \tag{6}$$

Thus, the vector $\overline{A''E''}$ is calculated as

$$\overline{A''E''} = \overline{A''O'} + \overline{O'O} + \overline{OF} + \overline{FT} + \overline{TE'} \tag{7}$$

in which $\overline{OO'}$ is the position vector of the UAV and $\overline{OF}$ is the position vector of the material deposition target, in respect to the global coordinate frame $\{\mathbb{O}\}$.

In order to control the motion of the moving platform in respect to the base of the Delta manipulator, the position vector

$\overline{A''E''}$ has to be expressed in its local frame at position A'', which can be calculated as

$$\overline{A''E''}_{A''} = \overline{\mathbf{Q}}_{O'}\ \overline{A''E''}\ \mathbf{Q}_{O'} \tag{8}$$

By using the kinematics solver and the position vector $\overline{A''E''}$ as derived above, the required input angles of the servos for the Delta manipulator can be computed. With the computed input angles, the end-effector of the Delta manipulator position at the target point by compensate for UAV's offsets.

This is a novel approach to compensating the UAV's offset in flight by using the advantages of a dexterous Delta manipulator.

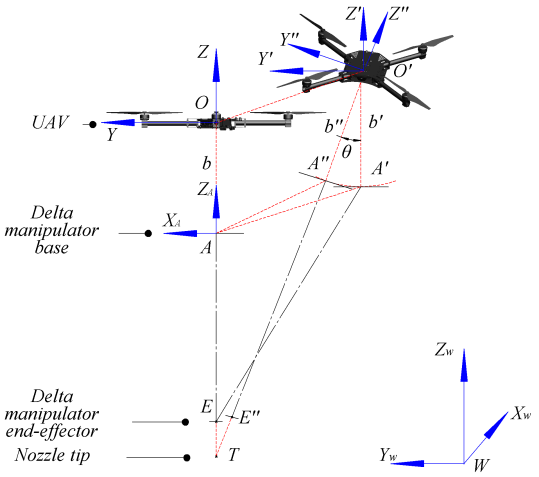

Fig. 4. The schematic drawing of the method for compensating UAV fluctuation using the integrated Delta manipulator.

III. Control Architecture of the Integrated Aerial Delta Manipulator

A. M100 control architecture

The Robot Operating System (ROS) has been chosen as our robotic middlware framework due to its widespread adoption in the robotics community, the features available and its ease of use. All of the packages mentioned below are either open-source ROS packages or implemented in ROS by us.

DJI M100 comes with DJI onboard SDK that allows users to communicate with its flight controller. In addition to this, we implemented a Model Predictive Controller(MPC) package from [26] to enable high-precision position control of the quadrotor UAV. A Multi Sensor Fusion(MSF) package from [27] has been used for the state estimation of the quadrotor UAV. This can follow position updates as input from either the motion capture system or the robot onboard VI odometry[28], outputing the position, orientation, velocity, angular velocity and linear and angular acceleration of the quadotor UAV that the MPC needs.

The motion capture system can generate a fixed inertial frame so that a fixed pose(position and orientation) setpoint can be used as the reference for the MPC position controller. However, when using VI odometry, the inertial frame shifts over time due to the lack of an online loop closure so that when a fixed setpoint is published to MPC, the quadrotor UAV still drifts slightly in its ground truth. To improve this, we used ARTag, which is a fiduciary marker system that supports augmented reality. An ARTag tracker package[29] is integrated to keep updating the ARTag position and orientation within the inertial frame. A trajectory publisher package is additionally implemented to update the pose setpoints that keep a constant position vector to the ARTag, enabling the ARTag to act as an anchor to stop the drift of M100.

B. Control System for the Delta Manipulator

The control flow diagram of the aerial robot with integrated Delta manipulator is illustrated in Fig. 5. Two ROS nodes have been programmed; (*i*) for inverse kinematic computation for the light-weight Delta manipulator as described in section II-B and (*ii*) for transmitting/receiving data packets with servo motors used in the joints of the Delta manipulator. We have implemented a modified Dynamixel SDK software system based on [30] to serve this purpose. To compensate for the UAV's offset from a desired trajectory, the real-time pose of the UAV, either from external motion capture system or VI odometry, and its trajectory command references are feed into ROS node for inverse kinematics computation. The controller for Delta manipulator is running alongside the MPC controller for the UAV.

C. Control System for the Extrusion Mechanism

In the extrusion system, an actuator is implemented to control the extrusion speed. The chosen motor (Dynamixel XL320) is a lightweight smart servo that has the suitable features and characteristics to perform as a joint in the Delta manipulator. However, it does not have a speed controller feature directly available. A closed-loop PID speed controller based on the encoder position data has been developed to resolve this issue.

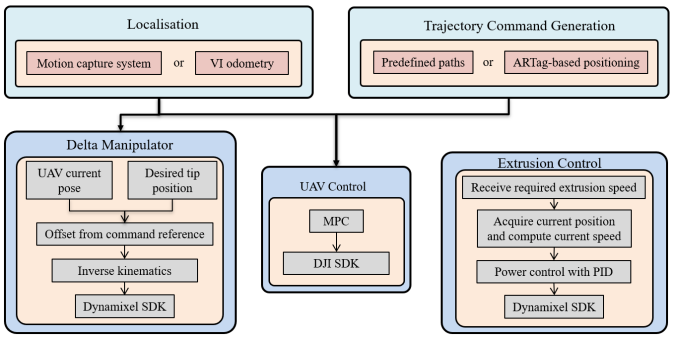

Fig. 5. Control diagram for the complete aerial robot with integrated Delta manipulator, material extrusion mechanism and VI sensor.

IV. Prototypes and Experimental Validation of Enhanced Stability

A. Hardware Setup

A DJI M100 quadrotor platform is used carrying a Intel®NUC7i7BNH (Intel®Core™i7-7567U Processor,

TABLE I
WEIGHT OF EACH ONBOARD COMPONENTS

Components	Weight [g]
DJI M100 quadrotor (with battery)	2350
Repair kit (without material)	250
Inter NUC	300
Intel Realsence ZR300	80
Delta manipulator module	220
Liquid expansion foam	35
Other accessories	235
Total	3500

16GB RAM and 250GB SSD) running Ubuntu 16.04 and ROS Kinetic. The robot also carries the repair kit and the custom-made Delta manipulator. The total mass of the system including liquid repair material is 3.5 kg with the masses of individual components listed in Table I. A Vicon motion capture system was used to provide 6-DOF pose feedback at 100 Hz for objects of interest within the flight arena. The PU foam extrusion system is controlled using 2.4 GHz RC link. Dynamixel XL320 smart servo has been chosen as the joints in the Delta manipulator due to its light weight at 16.7g each, its reliable digital communication rather than traditional PWM signal, the ease of its wiring in its ability to be connected within a daisy chain, and the PID tune-able position control mode. XL320 has also been used as the actuator for the extrusion mechanism and linked up to the daisy chain with servo motors in the Delta manipulator. Internal Dynamixel servo parameters have been fine-tuned to suit our applications.

B. Material deposition accuracy

As a criteria, we aim to be able to perform aerial repair works with end-effector positioning accuracy, including a maximum fluctuation in Z-axis of 20 mm or less to prevent the end-effector touching the repair surface. This is because the repairing nozzle head needs to be positioned in proximity to the repair surface in order to fully utilise the downwash windshield against the turbulence flow from the UAV propulsion system. Positioning in X-axis and Y-axis will benefit from improved accuracy; however, the required accuracy will depend on the size of the damaged area. Regardless of this, improving its accuracy means that the required LD40 PU foam volume will be minimised and will only be deposited in the vicinity of the area of interest. The LD40 PU foam has an large volume expansion ratio. With a mixture capable of 20 time expansion ratio, 0.02 ml of the mixture will generate a half sphere model with a radius of about 5.7mm, which is close to average size of single expanded foam droplet from empirical tests. This number will be used as a guideline for our X-axis and Y-axis root-mean-square-error (RMSE) accuracy evaluation in order to characterise whether or not the aerial material deposition can perform reliably at a given task.

C. UAV offset compensation with the Delta manipulator

A series of autonomous flight tests were conducted for demonstrating the ability of the system to position its end-effector accurately at a target point. To assess the performance of the end-effector stabilisation by the Delta manipulator, we tested the aerial robot in both still air and in a 1m/s windy condition. The wind is created by exposing the robot to a Drum Electric Fan generating 5500 cfm air flow directed at the robot while it hovers at spot $[0,0,1.5]^T$ m in the world frame.

TABLE II
PERFORMANCES OF THE AERIAL ROBOT IN VICON SPOT HOVERING

	RMSE (mm)		Decreases (%)	Max Fluctuations (mm)		Decreases (%)
	M100	Delta arm		M100	Delta arm	
X	5.52	1.74	68.5	10.84	4.89	54.9
Y	4.94	2.28	53.8	11.82	6.56	53.0
Z	10.43	1.94	81.4	22.32	5.72	74.4

TABLE III
PERFORMANCES OF THE AERIAL ROBOT IN VICON SPOT HOVERING WITH 1 m/s WIND ALONG Y-AXIS

	RMSE (mm)		Decreases (%)	Max Fluctuations (mm)		Decreases (%)
	M100	Delta arm		M100	Delta arm	
X	7.78	2.81	63.8	15.94	8.18	48.7
Y	22.12	5.19	76.5	52.07	11.67	77.6
Z	13.99	3.4	75.6	29.26	9.47	67.6

The test results of the aerial robot while it hovers in still air is given in Table II. As illustrated in Fig.6, the aerial robot using compensation function of the Delta manipulator is capable of decreasing both RMSE and the maximum fluctuations of the end-effector in all directions. The RMSEs decrease 68.5%, 53.8% and 81.4%, while the maximum fluctuations decrease 54.9%, 53.0% and 74.4% in X, Y, and Z direction respectively.

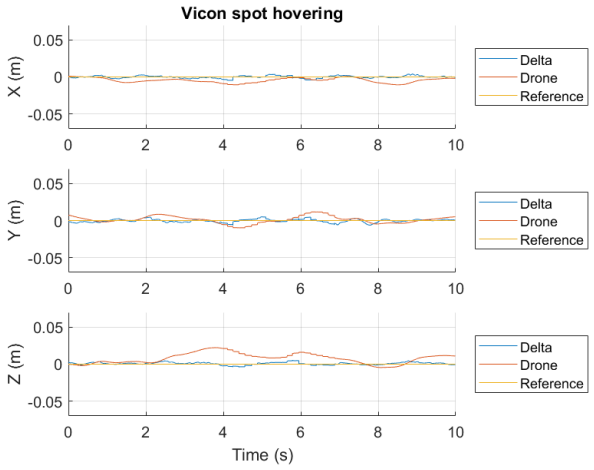

Fig. 6. Fluctuations from command reference level of the quadrotor platform and the end-effector of the integrated aerial robot in Vicon-based spot hovering mode.

In comparison to hovering in still air, the test results of the hovering aerial robot exposed a 1m/s windy condition with Y-direction wind generated by a Drum Electric Fan is given in Table III and illustrated in Fig.7. The results show that the Delta manipulator is able to compensate for the fluctuations of the quadrotor platform and decrease both RMSEs and maximum fluctuations of the end-effector in all directions. As given in Table III, the RMSEs decrease 63.8%, 76.5%

TABLE IV
PERFORMANCES OF THE AERIAL ROBOT IN VISUAL-INERTIAL SPOT HOVERING

	RMSE (mm)		Decreases (%)	Max Fluctuations (mm)		Decreases (%)
	M100	Delta arm		M100	Delta arm	
X	7.01	3.69	47.4	15.01	8.5	43.4
Y	7.18	5.32	25.9	16.08	13.71	14.7
Z	8.28	4.81	41.9	17.46	10.27	41.2

and 75.6%, while the maximum fluctuations decrease 48.7%, 77.6% and 67.6% in X, Y, and Z directions respectively.

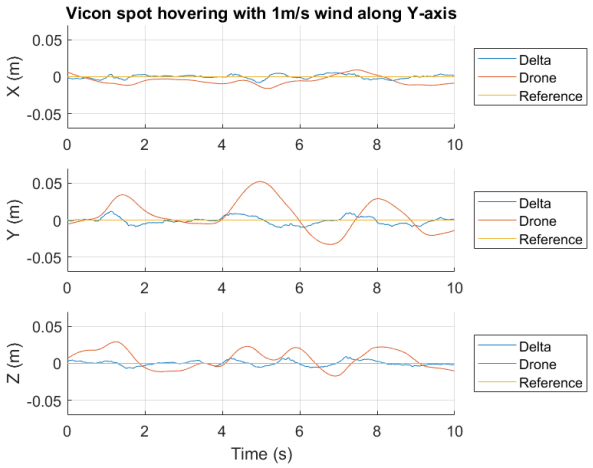

Fig. 7. Fluctuations from command reference level of the quadrotor platform and the end-effector of the integrated aerial robot in vicon based spot hovering mode with 1 m/s wind along Y-axis.

We further assessed the performance of the aerial robot using VI odometry-aided navigation by first hovering in still air and then in a windy environment. THe Vicon motion capture system is used to obtain the ground truth of the position of the end-effector and the quadrotor platform. The tests results of the aerial robot hovering in still air is given in Table IV and illustrated in Fig.8. In this operating scenario, the end-effector implements improved accuracy as the RMSEs decreased by 47.4%, 25.9% and 41.9%, while the maximum fluctuations decreased by 43.4%, 14.7% and 41.2% in X, Y, and Z direction respectively.

The results of the aerial robot exposed to Y-direction wind generated by the Drum Electric Fan is given in Table V. In this case, the end-effector also demonstrates improved accuracy (Fig.9) as the RMSEs decreased by 76.4%, 44.1% and 35.8%, while the maximum fluctuations decreased by 52.8%, 46.9% and 33.6% in X, Y, and Z direction respectively.

Across these four flight test scenarios, and in terms of targeted accuracy of Z-axis max fluctuation of 20 mm and X-axis and Y-axis RMSE of 5.7 mm, the aerial Delta Manipulator is able to pass the performance criteria in Vicon spot hovering, Vicon spot hovering with 1 m/s wind along Y-axis, and VI odometry spot hovering.

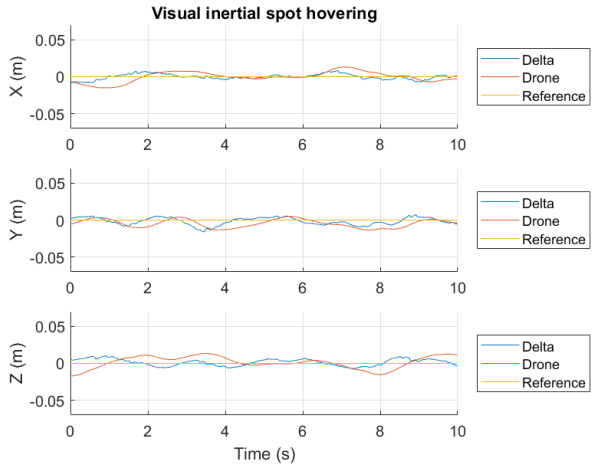

Fig. 8. Fluctuations from command reference level of the quadrotor platform and the end-effector of the integrated aerial robot in VI-odometry-aided spot hovering in still air.

TABLE V
PERFORMANCES OF THE AERIAL ROBOT IN VISUAL-INERTIAL SPOT HOVERING WITH $1m/s$ WIND ALONG Y-AXIS

	RMSE (mm)		Decreases (%)	Max Fluctuations (mm)		Decreases (%)
	M100	Delta arm		M100	Delta arm	
X	27.1	6.39	76.4	39.5	18.65	52.8
Y	26.46	14.77	44.1	78.14	41.52	46.9
Z	24.96	16.03	35.8	47.91	31.79	33.6

V. AERIAL REPAIR: PRECISE SEALING WITH AMORPHOUS CONSTRUCTION AND REPAIR MATERIALS

We designed an extrusion mechanism (Fig. 10) for depositing amorphous repair materials, such as LD40 Polyurethane foam, to effectively seal leaking spots including cracks and holes. Using two components PU foam has the advantage that the material properties can be easily modified.

A. The extrusion mechanism for material deposition

LD40 is a general-purpose two component PU form used in a wide range of applications. In light of properties of the material (LD40), it was adopted for this application due to its expansion rate of approx 20 times to it original volume. This relatively large volume change is advantageous for sealing purposes because the expansion can alleviate potential imprecision in the application process.

The extrusion mechanism consists of two 20 ml syringes for storing the two-part liquid components, a 3D printed mounting frame and laser machined spur gears for the power transmission. The syringes are modified by fixing the rubber plunger to the front tip of a lead-screw running through the centre of the syringe. The lead-screw is fixed with a captive nut embedded in the spur gear. The Dynamixel servo XL320 is selected for driving the spur gear train that will extrude the two components of the foam with the lead screw motion transmission mechanism.

A shorted pro epoxy mixer nozzle, with 15 acetal mixing elements and a total of 2.86 ml volume, is connected to two

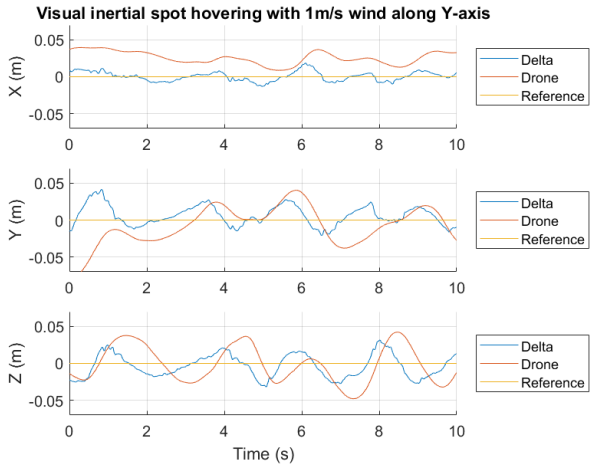

Fig. 9. Fluctuations from command reference level of the quadrotor platform and the end-effector of the integrated aerial robot in VI-odometry-aided spot hovering with 1 m/s wind along Y-axis.

flexible tubes with a Y-junction as shown in Fig. 10. A 3D printed conical wind shield is attached to the mixer nozzle to prevent the downwash wind that would affect the foam flow.

A control algorithm is then implemented to extrude materials and estimate the flow rate based on the angular velocity of the servo. By reversing the rotating direction of the servo, it allows the mechanism to refill the syringes with liquid PU foam material.

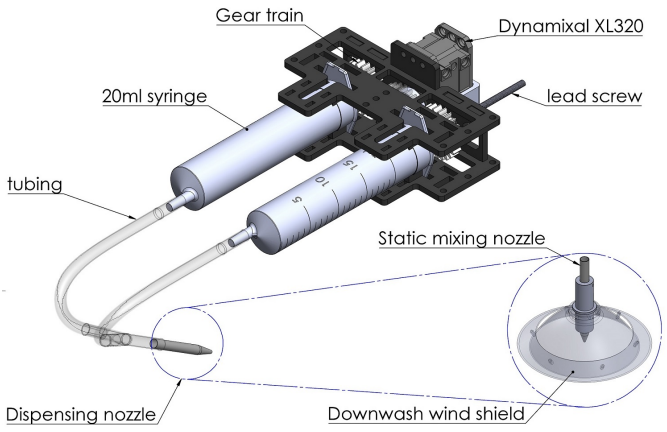

Fig. 10. The repairing kit with two-part PU foam material extruder and a static mixing nozzle.

B. Characterization of the LD40 polyurethane foam for autonomous deposition

To facilitate autonomous control of material deposition using the above extruding mechanism and complete aerial repair mission in a hard-to-reach position, we analysed the performance of the mixed foam quantitatively with experimental tests.

Given the volume of the nozzle, V_{nozzle}, used in the mechanism, the continuous flow rate Q through the nozzle is calculated by V_{nozzle}/t. To maintain this flow rate, the angular speed of the servo is derived as

$$\omega_m = \frac{2V_{nozzle}}{\pi t l {D_{syringe}}^2} \tag{9}$$

in which $R_{syringe}$ is the inner diameter of the 20ml syringe, t is the time required to drive the material out of the nozzle, and l is the lead of the screw thread.

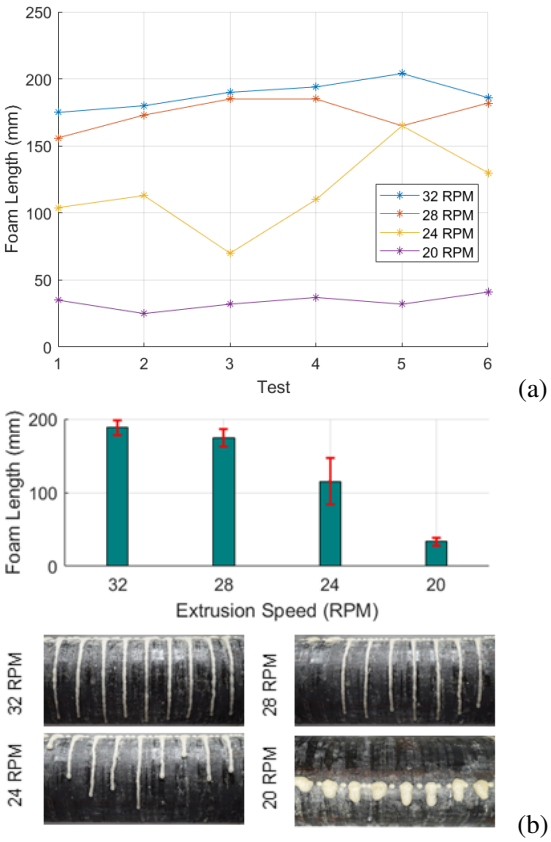

Fig. 11. The flowability of the mixture at various depositing flow rate on a pipe surface (a) length of the flow per test spot, (b) average length of the flow per extruding speed.

The cream-time of LD40 polyurethane foam is about 13-18 seconds, as given in the technical data sheet [31]. The material should therefore remain no longer than 18 seconds in the nozzle in order to drive the mixture out of the static mixing nozzle with little force. During this time we can assume that there is no significant change of viscosity of the mixture in the nozzle.

Substituting numerical values to Eq. 9, we derive a reference angular angular velocity of 32 rpm for the servo. By reducing the angular velocity, the flow rate of the two part foam material slows down and the mixture will become creamy within the nozzle. This further reduces the flowability of the mixture when it is deposited on an inclined surface.

To analyse the flowability of mixed LD40 foam at various depositing flow rates, we control the servo at different angular velocity starting from 32rpm, and continue to deposit material at spots on top of a standard steel pipe (D = 168mm) for 2 seconds at each spot. We then reduce the servo speed by equal

decrements of 4 rpm until the mixture doesn't flow down. The length of the flow down the pipe surface after setting is measured and reported in Fig. 11. The results reveal that the mixture deposited on top of the pipe will not flow down while the servo turns at less than 20 rpm.

The power for driving the PU foam out of the mechanism is provided by the Dynamixal servo. The mechanical power available from the gearbox output shaft is calculated by $\tau\omega$, where τ is the output torque and ω the angular velocity. Both the applied torque and real turning speed of the servo are readable with the control algorithm. For extruding tests at different extruding speeds without the static mixing nozzle, there are no significant changes for the required average torque output percentage, as shown in Fig. 12. After adding the mixing nozzle, the results reveal that to maintain a depositing flow rate with the servo turning at 32 rpm requires an increase of 20% torque output. These results also show that the lowest turning speed at 20 rpm requires an average of 15% torque output increase due to the higher viscosity of the mixture.

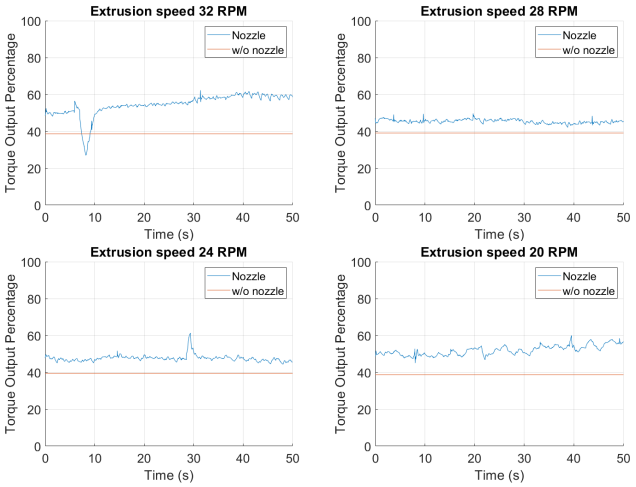

Fig. 12. Power consumption of the extrusion mechanism at various extruding speeds.

With the experimental results above, we can systematically control the servo velocity to have a mixture with higher flowability by increasing the extruding flow rate and thus a larger flow distance on the pipe surface. Conversely, a slower servo velocity leads to a mixture with higher viscosity and lower flowability, resulting in a creamier foam immediately after deposition.

C. Leaking sites sealing tests with autonomous flight

This preliminary experimental test is designed to implement aerial repair using the robotic system presented in this paper. In the test, a section of steel oil pipe with 168 mm diameter is used as a sample, on which a 15 mm straight line crack and another two 10 mm diameter leaking holes are assumed as repair targets.

The locations for the start and end point of the straight-line cracks and the centres of the two holes are obtained using the Vicon system before printing. Knowing these position vectors as key points in the coordinate frame of the Vicon system, a trajectory is then designed for autonomous flight with consideration to the maximum speed of DJI M100 and the distance between the tip of the nozzle and the pipe to avoid physical collision.

Given the fluctuation range of 0.0114 m in the vertical direction of the end-effector of the Delta manipulator, a minimum distance of 0.02 m is set between the tip of nozzle and the pipe as a buffer zone. With a number of flight tests for calibrating the practical flight trajectory, the distance between the mass centre of the drone and the surface of the steel pipe is established at 0.38 m.

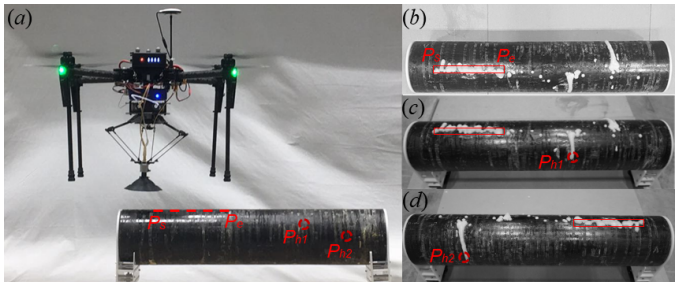

Fig. 13. The repair task setup and deposited PU foam for sealing cross-section crack between P_s and P_e and holes at P_{h1} and P_{h2}: (a) front view of the repair test, (b) top view of the expanded foam, (c-d) side view of the expanded foam at point P_{h1} and P_{h2}.

To implement the repair task, the aerial robot takes off from the side close to the starting point P_s and flies up to 1 m over the pipe. It then moves to the top of point P_s and consequently descends to the desired printing height as shown in Fig. 13(a). In this part, we adjust the velocity of the robot to match the required material depositing velocity, enabling the optimum repairing quality. After sealing the straight-line crack, the robot flies to points P_{h1} and P_{h2} and subsequently hovers over them to fill the two holes. After finishing the repair, the robot flies away from the work-site and lands on the right side of the pipe. Materials accumulated along the straight-line crack and holes on the pipe after the repair are shown in Fig.13 (b), (c) and (d).

During this test, the implemented trajectories of the M100 and the Delta manipulator are recorded in the motion capture environment and plotted with respect to their trajectory references as shown in Fig. 14.

A VI odometry-aided aerial repair work process is demonstrated in Fig. 15(a). In this repair process, the ARTag is placed in front of the repair target and a reference vector is calculated so that the target position of M100 is on the top of the repair target. M100 first flies to the standby position where the ARTag is in the view of the ZR300 camera, then the M100 begins to track the ARTag and maintain the constant reference vector with the ARTag. Once the target position is reached, the delta manipulator starts to stabilize the end-effector and the liquid expansion foam is extruded onto the repair targets precisely, as illustrated in Fig. 15(b).

VI. CONCLUSIONS

This work presents a new concept for precise aerial repair, including sealing and filling of cracks. An integrated light-weight 3-DOF Delta manipulator and closed-loop position

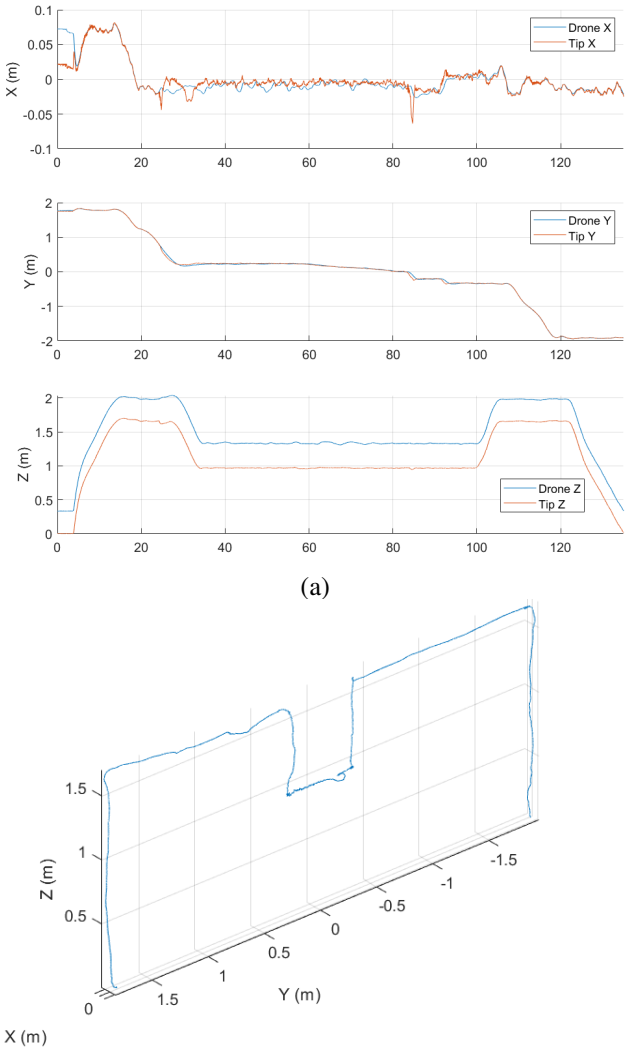

Fig. 14. Reference and implemented trajectories of the M100 and the end-effector of Delta manipulator in the pipeline repair process: (a) decomposed trajectories of the whole repair process along X-, Y- and Z-axis, (b) three dimensional trajectory of the planned repair process.

controller allows high-precision end-effector positioning on a UAV platform, showing higher precision than positioning the end effector with the UAV alone. Quantitative experimental data demonstrated that the integrated 3-DoF Delta manipulator is capable of compensating both the translation and rotation offset of the UAV frame, thereby achieving improved accuracy in all directions in the four no-wind and windy test scenarios. We present experimental demonstrations of pipeline repair and flat surface spot sealing by extruding LD40 polyurethane foam from the autonomous aerial robot. These tests verified the concept of using the proposed system for the repair of targets with different geometric shapes. This work can enable potential applications including accurate aerial inspection and repair for infrastructures in challenging environments, such as nuclear or petrochemical plants.

This work initiates a framework for implementing repair tasks at high altitude. Using the on-board camera, the potential of using this system to autonomously identify and repair a fault

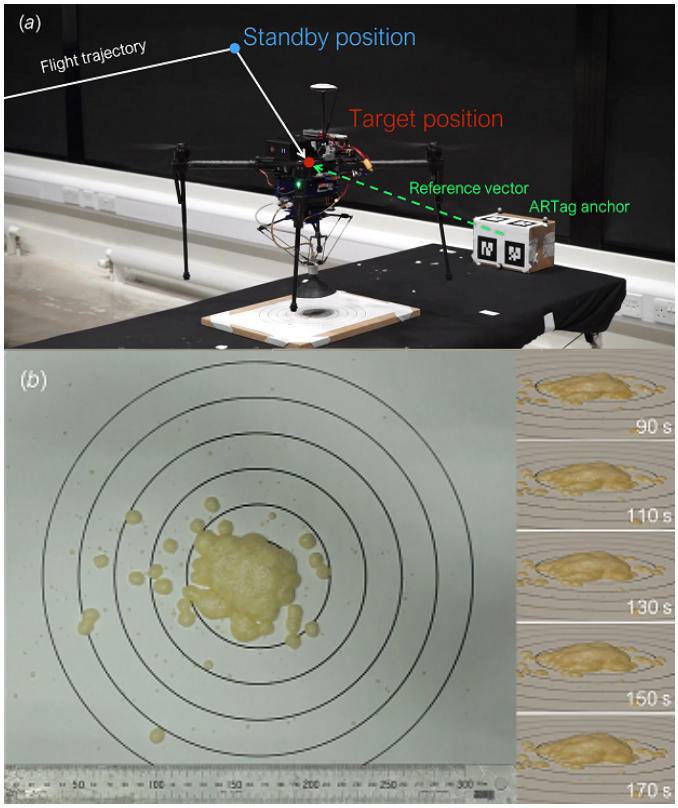

Fig. 15. The aerial repair mission using VI odometry-aided navigation. (a) the flight trajectory of the aerial robot for the aerial repairing process, (b) the foam material expansion progress in a period of 80 s after deposition at the target spot and the top view showing the final scale.

will be further investigated.

ACKNOWLEDGMENT

The authors would like to thank the supports of the EPSRC UK award under grant agreement EP/N018494/1, the Royal Thai Government Scholarship, the Royal Society Wolfson Fellowship under grant number RSWFR1180003 and the Department of Aeronautics of Imperial College London. We also thank Dr Talib Al-Hinai and Dr Robert Siddall for their contributions in the early stage of the Aerial Repair project[32].

REFERENCES

[1] D. Floreano and R. J. Wood, "Science, technology and the future of small autonomous drones," *Nature*, vol. 521, no. 7553, pp. 460–466, 2015.

[2] M. Kovac, "Learning from nature how to land aerial robots," *Science*, vol. 352, no. 6288, pp. 895–896, 2016.

[3] N. Kuntz and P. Oh, "Autonomous cargo transport system for an unmanned aerial vehicle, using visual servoing," in *Proceedings of the Cybernetics and Information Technologies, Systems and Applications Conference*, 2009, pp. 41–46.

[4] D. Axinte, X. Dong, D. Palmer, A. Rushworth, S. C. Guzman, A. Olarra, I. Arizaga, E. Gomez-Acedo, K. Txoperena, K. Pfeiffer *et al.*, "Mirorminiaturized robotic systems for holistic in-situ repair and maintenance works in restrained and hazardous environments," *IEEE/ASME Transactions on Mechatronics*, vol. 23, no. 2, pp. 978–981, 2018.

[5] M. Orsag, C. Korpela, and P. Oh, "Modeling and control of mm-uav: Mobile manipulating unmanned aerial vehicle," *Journal of Intelligent & Robotic Systems*, pp. 1–14, 2013.

[6] F. Ruggiero, M. A. Trujillo, R. Cano, H. Ascorbe, A. Viguria, C. Peréz, V. Lippiello, A. Ollero, and B. Siciliano, "A multilayer control for multirotor uavs equipped with a servo robot arm," in *Robotics and Automation (ICRA), 2015 IEEE International Conference on*. IEEE, 2015, pp. 4014–4020.

[7] S. Moe, G. Antonelli, A. R. Teel, K. Y. Pettersen, and J. Schrimpf, "Set-based tasks within the singularity-robust multiple task-priority inverse kinematics framework: General formulation, stability analysis, and experimental results," *Frontiers in Robotics and AI*, vol. 3, p. 16, 2016.

[8] G. Muscio, F. Pierri, M. A. Trujillo, E. Cataldi, G. Antonelli, F. Caccavale, A. Viguria, S. Chiaverini, and A. Ollero, "Coordinated control of aerial robotic manipulators: Theory and experiments," *IEEE Transactions on Control Systems Technology*, pp. 1–8, 2017.

[9] D. Mellinger, Q. Lindsey, M. Shomin, and V. Kumar, "Design, modeling, estimation and control for aerial grasping and manipulation," in *2011 IEEE/RSJ International Conference on Intelligent Robots and Systems*. IEEE, 2011, pp. 2668–2673.

[10] P. E. I. Pounds, D. R. Bersak, and A. M. Dollar, "The yale aerial manipulator: Grasping in flight," in *2011 IEEE International Conference on Robotics and Automation*, 2011, pp. 2974–2975.

[11] J. Thomas, G. Loianno, J. Polin, K. Sreenath, and V. Kumar, "Toward autonomous avian-inspired grasping for micro aerial vehicles," *Bioinspiration & biomimetics*, vol. 9, no. 2, p. 025010, 2014.

[12] D. Mellinger, M. Shomin, N. Michael, and V. Kumar, "Cooperative grasping and transport using multiple quadrotors," in *Distributed autonomous robotic systems*. Springer, 2013, pp. 545–558.

[13] K. Baizid, G. Giglio, F. Pierri, M. A. Trujillo, G. Antonelli, F. Caccavale, A. Viguria, S. Chiaverini, and A. Ollero, "Experiments on behavioral coordinated control of an unmanned aerial vehicle manipulator system," in *Robotics and Automation (ICRA), 2015 IEEE International Conference on*. IEEE, 2015, pp. 4680–4685.

[14] M. Orsag, C. Korpela, S. Bogdan, and P. Oh, "Valve turning using a dual-arm aerial manipulator," in *Unmanned Aircraft Systems (ICUAS), 2014 International Conference on*. IEEE, 2014, pp. 836–841.

[15] S. Kim, S. Choi, and H. J. Kim, "Aerial manipulation using a quadrotor with a two dof robotic arm," in *Intelligent Robots and Systems (IROS), 2013 IEEE/RSJ International Conference on*. IEEE, 2013, pp. 4990–4995.

[16] C. Gosselin and J. Angeles, "The optimum kinematic design of a spherical three-degree-of-freedom parallel manipulator," *Journal of mechanisms, transmissions, and automation in design*, vol. 111, no. 2, pp. 202–207, 1989.

[17] J.-P. Merlet, *Parallel robots*. Springer Science & Business Media, 2006, vol. 128.

[18] A. Hernández, O. Altuzarra, O. Salgado, C. Pinto, and V. Petuya, "Designing parallel manipulators: from specifications to a real prototype," *Industrial Robot: An International Journal*, vol. 39, no. 5, pp. 500–512, 2012.

[19] R. Cano, C. Pérez, F. Pruano, A. Ollero, and G. Heredia, "Mechanical design of a 6-dof aerial manipulator for assembling bar structures using uavs," in *2nd RED-UAS 2013 workshop on research, education and development of unmanned aerial systems*, 2013.

[20] "Drones that fix pipeline leaks win international acclaim," https://www.imperial.ac.uk/news/170806/drones-that-pipeline-leaks-international-acclaim/, accessed: 2018-02-10.

[21] G. Hunt, F. Mitzalis, T. Alhinai, P. A. Hooper, and M. Kovac, "3d printing with flying robots," in *Robotics and Automation (ICRA), 2014 IEEE International Conference on*. IEEE, 2014, pp. 4493–4499.

[22] F. Pierrot, C. Reynaud, and A. Fournier, "Delta: a simple and efficient parallel robot," *Robotica*, vol. 8, no. 2, pp. 105–109, 1990.

[23] S. Staicu and D. C. Carp-Ciocardia, "Dynamic analysis of clavel's delta parallel robot," in *2003 IEEE International Conference on Robotics and Automation (Cat. No.03CH37422)*, vol. 3, no. 3, Sept 2003, pp. 4116–4121.

[24] X. Yang, Z. Feng, C. Liu, and X. Ren, "A geometric method for kinematics of delta robot and its path tracking control," in *Control, Automation and Systems (ICCAS), 2014 14th International Conference on*. IEEE, 2014, pp. 509–514.

[25] "Delta robot kinematics," http://hypertriangle.com/ alex/delta-robot-tutorial/, accessed: 2017-09-10.

[26] I. Sa, M. Kamel, R. Khanna, M. Popovic, J. Nieto, and R. Siegwart, "Dynamic system identification, and control for a cost effective open-source vtol mav," *arXiv preprint arXiv:1701.08623*, 2017.

[27] S. Lynen, M. Achtelik, S. Weiss, M. Chli, and R. Siegwart, "A robust and modular multi-sensor fusion approach applied to mav navigation," in *Proc. of the IEEE/RSJ Conference on Intelligent Robots and Systems (IROS)*, 2013.

[28] T. Schneider, M. T. Dymczyk, M. Fehr, K. Egger, S. Lynen, I. Gilitschenski, and R. Siegwart, "maplab: An open framework for research in visual-inertial mapping and localization," *IEEE Robotics and Automation Letters*, 2018.

[29] "ar_track_alvar - ROS Wiki." [Online]. Available: http://wiki.ros.org/ar_track_alvar

[30] "Robotis git," https://github.com/ROBOTIS-GIT/, accessed: 2018-02-10.

[31] "Ld40 polyurethane - hard foam," http://www.mbfg.co.uk/foam-materials/foam-hard.html/, accessed: 2018-02-10.

[32] "Drones that fix pipeline leaks win international acclaim," https://www.imperial.ac.uk/news/170806/drones-that-pipeline-leaks-international-acclaim/, accessed: 2018-12-10.

Pisak Chermprayong, Aerial Robotics Lab(ARL), Department of Aeronautics, Imperial College London, South Kensington Campus, London, SW7 2AZ United Kingdom. Email: pisak.chermprayong10@imperial.ac.uk.

Ketao Zhang, Aerial Robotics Lab(ARL), Department of Aeronautics, Imperial College London, South Kensington Campus, London, SW7 2AZ United Kingdom. Email: ketao.zhang@qmul.ac.uk, ketao.zhang@imperial.ac.uk.

Feng Xiao, Aerial Robotics Lab(ARL), Department of Aeronautics, Imperial College London, South Kensington Campus, London, SW7 2AZ United Kingdom. Email: feng.xiao16@imperial.ac.uk.

Mirko Kovac, Director of the Aerial Robotics Lab(ARL), Department of Aeronautics, Imperial College London, South Kensington Campus, London, SW7 2AZ United Kingdom. Email: m.kovac@imperial.ac.uk.